

CLUMP DEVELOPMENT BY THE NICKEL BUBBLE EFFECT IN SUPERNOVAE

Chih-Yueh Wang

*Department of Astronomy and Astrophysics
University of California at Santa Cruz
UCO/Lick, 1156 High Street, Santa Cruz, CA 95064
E-mail: yueh@ucolick.org*

ABSTRACT

We used one-dimensional radiative-transport radiation hydrodynamical simulations to investigate the formation of clumping in freely-expanding supernova ejecta due to the radioactive heating from the $^{56}\text{Ni} \rightarrow ^{56}\text{Co} \rightarrow ^{56}\text{Fe}$ decay sequence. The heating gives rise to an inflated Nickel bubble, which induces a forward shock that compresses the outer ambient gas into a shell. The radiative energy deposited by the radioactivity leaks out across the shock by radiative diffusion, and we investigate its effect on the evolution of the ejecta structure. Compared to the hydrodynamical adiabatic approximation with $\gamma = 4/3$, the preshock gas becomes accelerated by the radiation outflow. The shock is thus weakened and the shell becomes broader and less dense. The thickness of the shell takes up $\lesssim 4\%$ of the radius of the bubble, and the structure of the shell can be approximately described by a self-similar solution. We compared the properties of the shell components with those of the ejecta clumps indicated by our previous hydrodynamical simulations for the later interaction of clumps with the outer supernova remnant. There is insufficient gas at high density contrast to cause a pronounced protrusion on the outline of a remnant, like the bullets in the Vela supernova remnant.

Subject headings: radiative transfer — supernova remnants — supernovae: general

1. INTRODUCTION

Observations of SN 1987A showed that the distribution of Fe in the ejecta is not what would be expected in the simplest models: it extended to higher velocity than expected and

had a large filling factor for its mass of $0.07M_{\odot}$ determined from the supernova light curve (McCray 1993; Li, McCray, & Sunyaev 1993). A plausible mechanism for the large filling factor is the Ni bubble effect, in which the radioactive progenitors of the Fe expand relative to their surroundings because of the radioactive power deposition (Woosley 1988; Li et al. 1993; Basko 1994). This effect is important during the first ~ 10 days after the supernova, when the radioactive power is significant and the diffusion of energy is not yet an important process.

An expected effect of the Ni bubble expansion is to create clumps in the nonradioactive gas. There is widespread evidence that the ejecta of core collapse supernovae are clumpy. The oxygen line profiles in the nearby Type II supernovae SN 1987A (Stathakis et al. 1991) and SN 1993J (Spyromilio 1994; Matheson et al. 2000) showed evidence for structure, implying that the gas is clumped. The velocity range for the emission extends to $1,500 \text{ km s}^{-1}$ in SN 1987A and $-4,000 \text{ km s}^{-1}$ in SN 1993J. Similar evidence for clumping has been found in the Type Ib supernova SN 1985F (Filippenko & Sargent 1989). Among young supernova remnants, Cas A is the prototype of the oxygen-rich SNRs, which show evidence for freely expanding, oxygen-rich ejecta in clumps. Puppis A, with an age $\sim 3,700$ yr, is a more elderly example of such a remnant (Winkler et al. 1988).

Wang & Chevalier (2001, 2002, hereafter WC01, WC02) investigated the role of clumps in the evolution of supernova remnants. In Tycho’s remnant, believed to be the remnant of a Type Ia supernova, the presence of ejecta knots near the outer shock front requires a density contrast $\chi \gtrsim 100$ relative to the surrounding ejecta (WC01). The remarkable protrusions in the X-ray image of the Vela remnant are likely to be caused by ejecta clumps (Aschenbach et al. 1995) and WC02 found that $\chi \sim 1000$ is needed to create the structures. The free expansion velocities for the clumps were estimated at $\sim 3,000 \text{ km s}^{-1}$.

Our aim here is to investigate whether the Ni bubble effect can cause the clump structure apparently needed in the Tycho and Vela remnants. We compute one-dimensional hydrodynamical calculations, building on the work of Basko (1994). We extend Basko’s work by including the effects of radiative diffusion and by carefully examining the density structure of the shell swept up by the Ni bubble. We show our computational setup and methods in § 2. The solutions for radiation-hydrodynamical effects are given in § 3. We also draw on the analogy to power input in a pulsar bubble to provide insight into the shell structure and evolution. In § 4 and § 5, we discuss the radiative effects on the Rayleigh-Taylor instabilities of the Ni bubble shell and the inferred ejecta-clump properties.

2. INITIAL CONDITIONS AND METHODS

We consider all of the ^{56}Ni synthesized in a supernova explosion initially resides in an isolated sphere in the center of supernova ejecta, with a mass M_{Ni} and a density contrast ω relative to the surrounding diffuse ejecta. The total radioactive energy released in the $^{56}\text{Ni} \rightarrow {}^{56}\text{Co} \rightarrow {}^{56}\text{Fe}$ decay sequence is deposited at a rate $q(t)$ (Basko 1994)

$$q(t) = \frac{Q_{Ni}}{t_{Ni}} \exp\left(-\frac{t}{t_{Ni}}\right) + \frac{Q_{Co}}{t_{Co}} \frac{\exp(-t/t_{Co}) - \exp(-t/t_{Ni})}{1 - t_{Ni}/t_{Co}},$$

where t_{Ni}, t_{Co} and Q_{Ni}, Q_{Co} are, respectively, the mean life and specific decay energy of $^{56}\text{Ni}, {}^{56}\text{Co}$:

$$\left. \begin{array}{l} t_{Ni} = 7.6 \times 10^5 \text{ sec} = 8.8 \text{ days} \\ Q_{Ni} = 2.14 \text{ MeV/decay} = 3.69 \times 10^{16} \text{ ergs g}^{-1} \end{array} \right\} {}^{56}\text{Ni} \rightarrow {}^{56}\text{Co}$$

$$\left. \begin{array}{l} t_{Co} = 9.64 \times 10^6 \text{ sec} = 111.5 \text{ days} \\ Q_{Co} = 7.87 \text{ Mev/decay} = 7.87 \times 10^{16} \text{ ergs g}^{-1}. \end{array} \right\} {}^{56}\text{Co} \rightarrow {}^{56}\text{Fe}$$

The accumulation of the total radioactive energy rises from 10^4 sec and saturates at $\gtrsim 10^7$ sec (Fig. 1) Before the saturation point is reached, the radioactive energy can leak out of the bubble by radiative diffusion. This can occur while the gas remains optically thick to the ~ 1 MeV γ -rays.

We assume that the diffuse supernova ejecta are initially freely-expanding so that each gas element moves with a constant velocity $v = r/t$. The part of the ejecta unaffected by the radioactivity has its density drop as t^{-3} , and the pressure drops as t^{-4} for a $\gamma = 4/3$, radiation dominated fluid. We refer our simulation initial conditions to Basko's parameters for SN 1987A (Basko 1994 and the references therein):

$$M_{Ni} = 0.075 M_{\odot}, \quad \omega = 3$$

$$t_0 = 10^4 \text{ sec}, \quad \rho_{a0} = 10^{-4} \text{ g cm}^{-3}, \quad P_0 = 2.5 \times 10^{11} \text{ dyn cm}^{-2},$$

where t_0 , ρ_{a0} and P_0 are the initial age, ejecta substrate density (surrounding the bubble), and background pressure, respectively. The initial velocity at the bubble edge $r = R_0$ is given by the initial Ni density contrast and age:

$$U_0 = \frac{R_0}{t_0} = \left(\frac{3M_{Ni}}{4\pi\rho_{Ni}} \right)^{1/3} \frac{1}{t_0} = 7 \times 10^7 \omega^{-1/3} \text{ cm s}^{-1}.$$

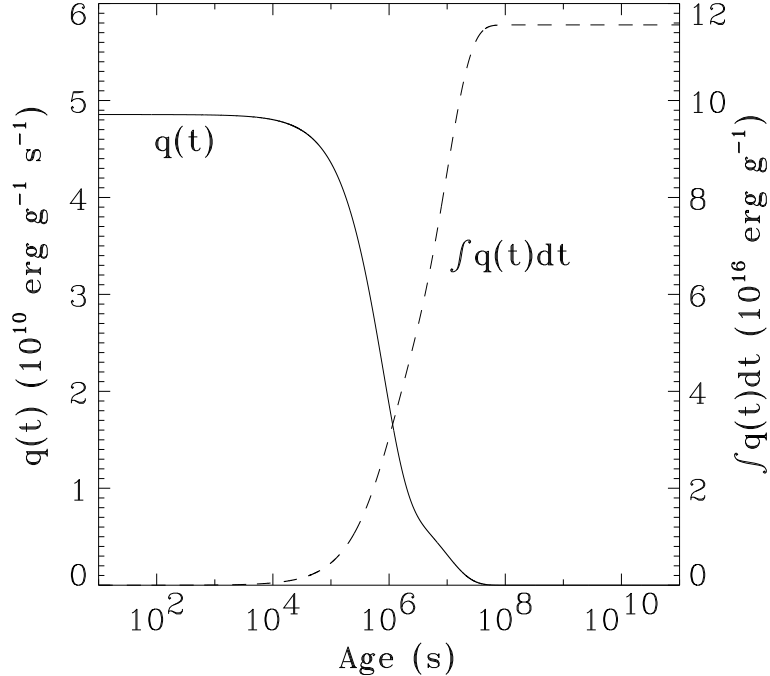


Fig. 1.— Evolution of the instantaneous and accumulated heating rate of the Nickel and Cobalt radioactive decay.

For $\omega = 3$, $R_0 = 5.0 \times 10^{11}$ cm. The initial pressure is assumed uniformly distributed inside and outside the bubble, independent of the bubble size. The pressure in the Ni bubble is determined by the radioactive power input at later times.

We note that the above parameters give an ejecta structure comparable to the inner flat-density component of the outer power-law ejecta density model that has a power index $n = 8$ ($\rho \propto r^{-n}$ in the outer parts), an ejecta mass $M = 10 M_\odot$, and an explosion energy $E = 10^{51}$ ergs (Chevalier & Liang 1989). The transition between the flat and power law parts of the density profile occurs at $v = 3162$ km s $^{-1}$ for these parameters. This set of explosion conditions is suitable for core-collapse supernovae and had been used in our two-dimensional hydrodynamical simulations for the Vela supernova remnant (WC02). The energy density is initially dominated by the energy deposited by the supernova shock. Shigeyama & Nomoto's (1990, their Fig. 2) model for SN 1987A indicates an adiabat $\kappa = 6.3 \times 10^{15}$ (cgs units) where $P = \kappa \rho^\gamma$; for $t_0 = 10^4$ sec, $\rho_0 = 9.4 \times 10^{-5}$ g cm $^{-3}$ in our density model, and so $P_0 = 2.7 \times 10^{10}$ dynes cm $^{-2}$. We take $P_0 = 2.7 \times 10^{10}$ dynes cm $^{-2}$ as the appropriate value at 10^4 sec. The time to set up the free expansion phase depends on the radius of the star because of the effects of reverse shock waves. For a blue supergiant progenitor star, like that of SN 1987A, the timescale is $\sim 10^4$ sec; for a red supergiant progenitor, the timescale is $\sim 10^5$ sec.

We first approach the problem using hydrodynamical simulations with $\gamma = 4/3$ in both the bubble interior and the ejecta substrate. We follow the bubble-shell interface on a spherical expanding grid, and add the specific radioactive energy to the internal energy within the bubble uniformly and locally, i.e., in proportion to the local mass density. We use a reflecting condition for the inner boundary, and apply a non-zero gradient outflow condition on the outer boundary to eliminate the spurious shock raised by the grid expansion. We find the saturated solution of the ejecta structure is independent of the initial density contrast ω or age t_0 , given a nickel mass. Also, the background pressure is unimportant if the initial radiation pressure from radioactivity dominates. In the case that the initial background pressure exceeds the accumulated pressure from radioactivity, the shell takes more time to build up, but the solution gradually converges once the radioactive energy input becomes dominant.

We include radiation hydrodynamics (RHD) in the simulations using the ZEUS2D code (Stone, Mihalas, & Norman 1992). The radioactive power is deposited into the radiation instead of the material and $\gamma = 5/3$ for the matter. The code is based on finite difference and finite volume on an Eulerian grid and uses an artificial viscosity to smooth shock transitions. The RHD algorithm treats nonrelativistic full radiative transport, under the assumption of LTE (local thermal equilibrium) and gray opacity. In our situation, the radiation effects are important when the gas is still optically thick, so that the diffusion approximation is adequate for the radiation transport. At the times of interest for the nickel bubble, the opacity is dominated by electron scattering. For completely ionized heavy elements the Thompson scattering mass opacity is $\sim 0.2 \text{ cm}^2 \text{ g}^{-1}$. For the case without absorption, we have calculated the cases with the initial energy being equally partitioned between radiation and material, or being dominated by either one. We find that our results are insensitive to the initial distribution of energy.

3. SHELL STRUCTURE AND EVOLUTION

3.1. Simulations

We show in Figs. 2 and 3 the ejecta structure on the flat density component of the power-law model $n = 8$, $E = 10^{51} \text{ erg s}^{-1}$, and $M = 10 M_\odot$. These simulations were initiated with $t_0 = 10^2 \text{ sec}$, $M_{Ni} = 0.075 M_\odot$ and $\omega = 3$; the diffuse ejecta have an initial density $\rho_0 = 94.4 \text{ g cm}^{-3}$ and an accumulated radioactive energy density $e_{rad0} = 1.38 \times 10^{15} \text{ erg cm}^{-3}$. The opacity is determined by electron scattering; the initial material and radiation energy density in the background are equally divided, $e_0 = e_{r0} = 1.35 \times 10^{10} \text{ erg cm}^{-3}$.

We first examined the evolution of the flow in the purely hydrodynamic simulations.

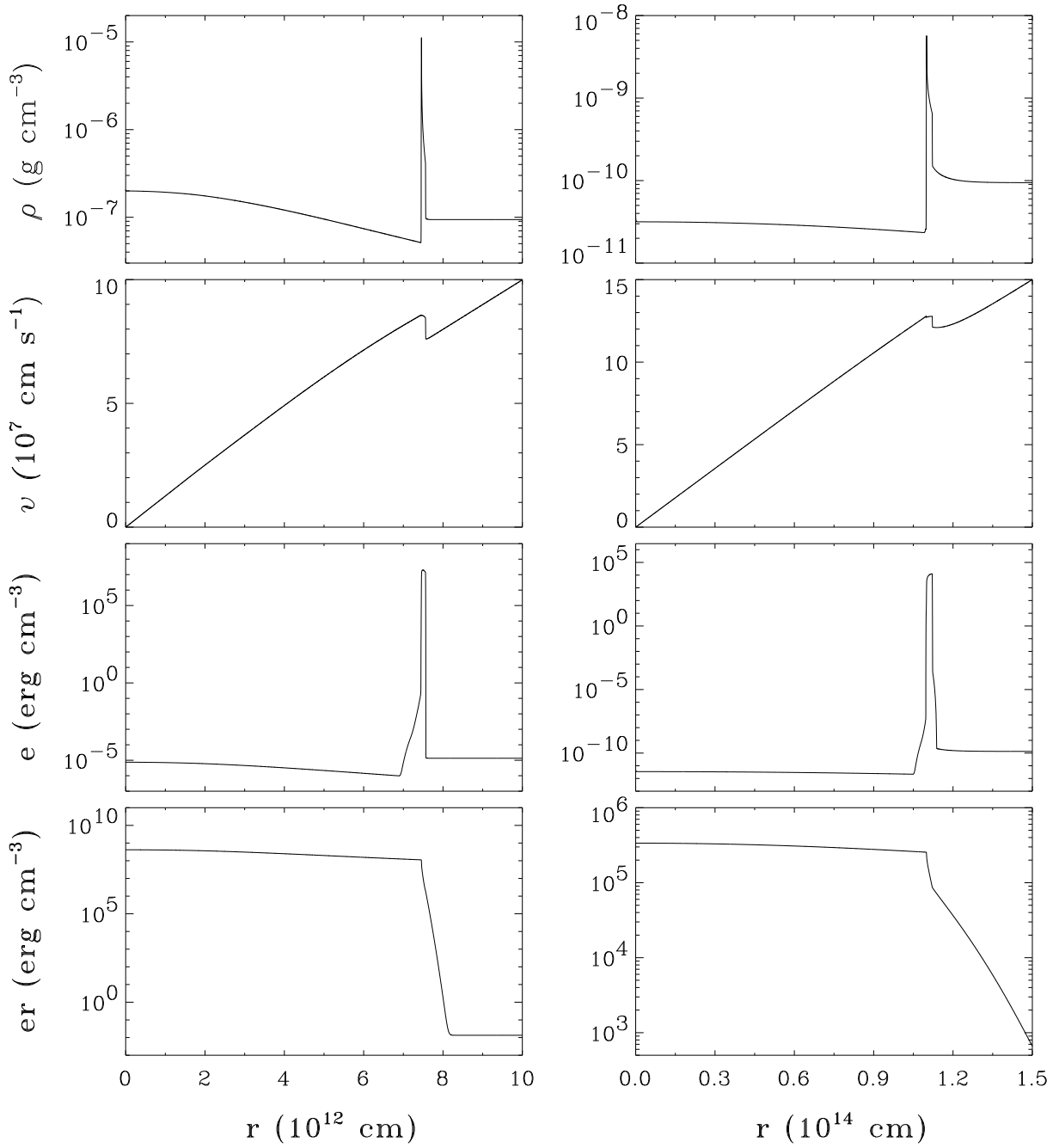


Fig. 2.— Distributions of density, velocity, gas energy density, and radiation energy density of the Nickel bubble structure in the flat-density ejecta of the power-law model at 10^5 and 10^6 sec. The initial Nickel mass is $M_n = 0.075 M_\odot$. The grid has 8000 uniform zones that resolve the shell into ~ 100 zones.

The expansion of the bubble gives rise to a strong forward shock behind which the ambient gas is compressed into a dense shell (Figs. 2 and 3). The inner edge of the shell is a contact discontinuity where the gas comoves with the bubble-shell interface; it has a high density because of the acceleration of the shell. To describe the acceleration, we use $a \equiv (dR_{sh}/dt)/(R_{sh}/dt)$, the expansion rate evaluated at the shock front R_{sh} , equivalent to the velocity ratio of the shell to the preshock diffuse ejecta. We find that a rises to a maximum $\lesssim 1.20$ around $\lesssim 10^6$ sec, and subsequently tends to 1.0 at late times as the shell becomes comoving with the preshock gas (Fig. 6). Because the background pressure has little influence on the dynamics, the shell structure becomes frozen into the flow.

The shell is very thin, with a thickness as a fraction of the shell $\beta \equiv h_{sh}/R_{sh} \lesssim 0.02$, where R_{sh} and h_{sh} are respectively the radius and thickness of the shell. The initial shock compression is set by the jump condition

$$\frac{\rho_1}{\rho_0} = \frac{(\gamma + 1)\mathcal{M}^2}{(\gamma - 1)\mathcal{M}^2 + 2}, \quad (1)$$

where

$$\mathcal{M} = \frac{v_{sh}}{c_0} = \left(\frac{dR_{sh}}{dt} - \frac{R_{sh}}{t} \right) \left(\frac{\rho_0}{\gamma p_0} \right)^{1/2} \quad (2)$$

is the Mach number of the shock, ρ_1 is the postshock density, v_{sh} is the shock velocity relative to the preshock gas, and c_0 is the sound speed in the preshock medium. For a radiation dominated, strong shock, $\rho_1/\rho_0 = 7$. The accelerating shell has a higher density in the postshock region so that a typical compression factor in the shell (relative to the preshock gas) is $\chi \sim 10$. We note that $\beta \approx (3\chi)^{-1}$. The highest density occurs at the inner edge, where the density is limited by the numerical resolution (Fig. 3).

In the RHD case, the energy from the heated gas leaks out from the bubble energy reservoir as time progresses (Fig. 3). The gas is radiation dominated. Radiative diffusion allows the internal energy to propagate ahead of the shock wave, and so eliminates the temperature and the radiation pressure gradients. In order for diffusion to be dynamically important, it requires that the diffusion time scale, t_d , be smaller than the hydrodynamic time scale of the flow, t_h ; i.e.,

$$t_d \approx \frac{h_{sh}^2}{\lambda c} < t_h \approx \frac{h_{sh}}{v_{sh}} \quad (3)$$

where λ is the photon mean free path. We note that

$$\frac{t_d}{t_h} \approx \left(\frac{h_{sh}}{\lambda} \right) \left(\frac{v_{sh}}{c} \right). \quad (4)$$

At $t \approx 3 \times 10^6$ s, $h_{sh} = 10^{13}$ cm, $\lambda = 1/\kappa\rho = 5 \times 10^{10}$ cm, so that $t_d = h_{sh}^2/\lambda c = 6 \times 10^4$ sec. At this time, $v_{sh} \approx 1 \times 10^7$ cm s⁻¹, so $t_d/t_h \approx 0.07$. The gas is optically thick, but

radiative diffusion is important. As a result of diffusion, the preshock gas is accelerated by the radiation; the shock is then weakened. The shock front develops a radiative precursor (Fig. 3). The acceleration of the bubble shell is reduced because of the radiative loss. The rise in the preshock sound speed and the acceleration of gas ahead of the shock reduced the sound speed and the shock compression (eqn. [1]). The shell becomes broader and less dense compared to the HD case. The sharp density jump at the shock front in the HD case is also smoothed out before the gradient of e_r diminishes to zero. The gas tends toward a freely expanding state in which the density profile is frozen into the flow.

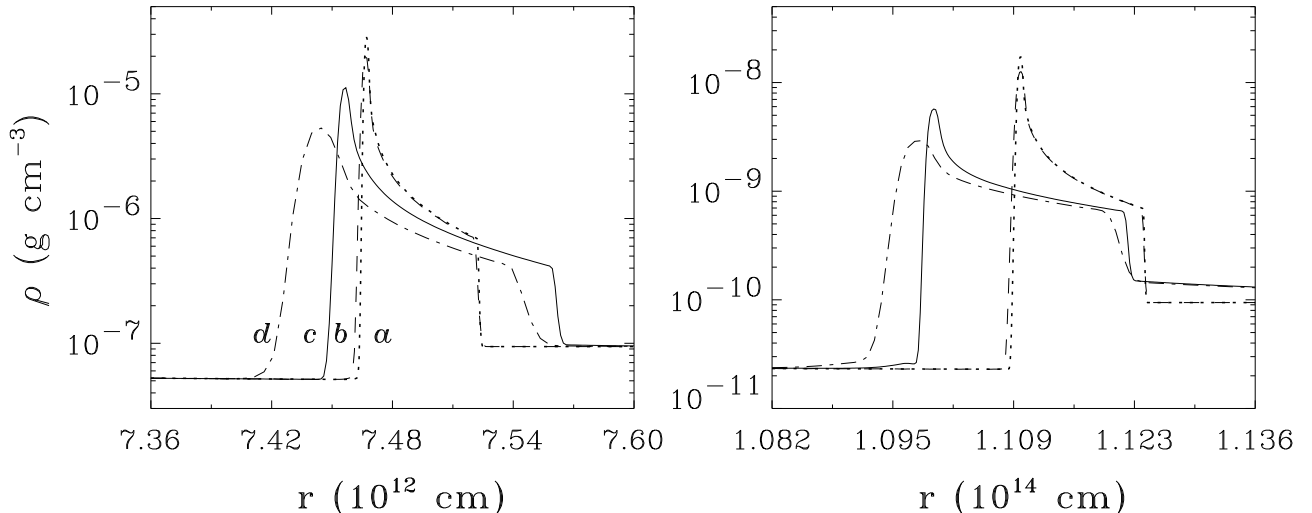


Fig. 3.— Density profiles of the Nickel bubble shell at 10^5 and 10^6 sec. a: HD solution on a nonuniform grid of 8000 zones that resolves the shell into 200 zones. b: HD solution on a uniform grid of 8000 zones. c: RHD solution on a uniform grid of 8000 zones. d: RHD solution on a uniform grid of 2000 zones.

The diffusion effect speeds up the freeze-out of the ejecta structure. For our parameters, the freezing occurs at a velocity $v_f \sim 1500 \text{ km s}^{-1}$ and a time $t_f \sim 10^7 \text{ s}$, significantly earlier than the HD case where $t_f \sim 10^9 \text{ sec}$ and $v_f \sim 1900 \text{ km s}^{-1}$. Both cases show a density contrast $\chi \gtrsim 10$ between the shell and the preshock ejecta. The inner edge (contact discontinuity) of the shell is the densest with $\chi \gtrsim 100$. The shell thickness is increased to $\sim 4\%$ of the radius of the bubble. The swept-up mass in the shell is about $M_s = 1M_\odot$. Note that we define the thickness as the distance from the contact discontinuity to the postshock outer dense region at the shock front, considering that the outermost postshock density profile flattens out into the ejecta substrate. When the initial Nickel mass is increased to 3 times $0.075 M_\odot$, the onset of freezing is delayed to $t_f \sim 10^8 \text{ sec}$ with $v_f \sim 1800 \text{ km s}^{-1}$ and $M_s \lesssim 3M_\odot$. For a 10 times increase, $t_f \sim 10^8 \text{ s}$, $v_f \sim 2400 \text{ km s}^{-1}$, and $M_s \lesssim 16M_\odot$. It is

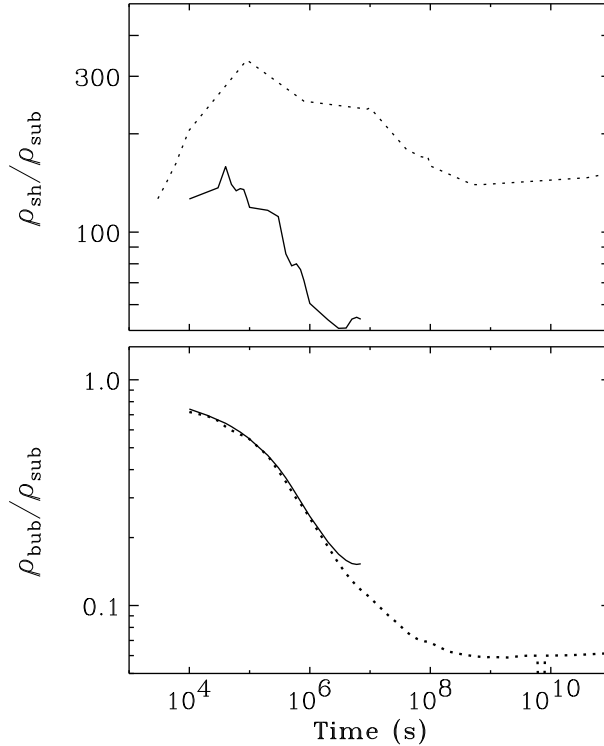


Fig. 4.— Top: Evolution of the density contrast between the densest region in the shell and the ejecta substrate. Bottom: Evolution of the density contrast between the bubble and the ejecta substrate. Solid and dotted lines represent the RHD and the HD case, respectively.

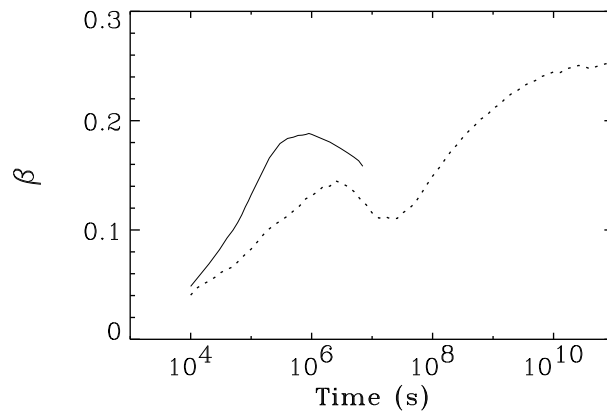


Fig. 5.— Evolution of the thickness ratio β of the shell. The value is influenced by numerical resolution. Solid line: RHD; dotted line: HD.

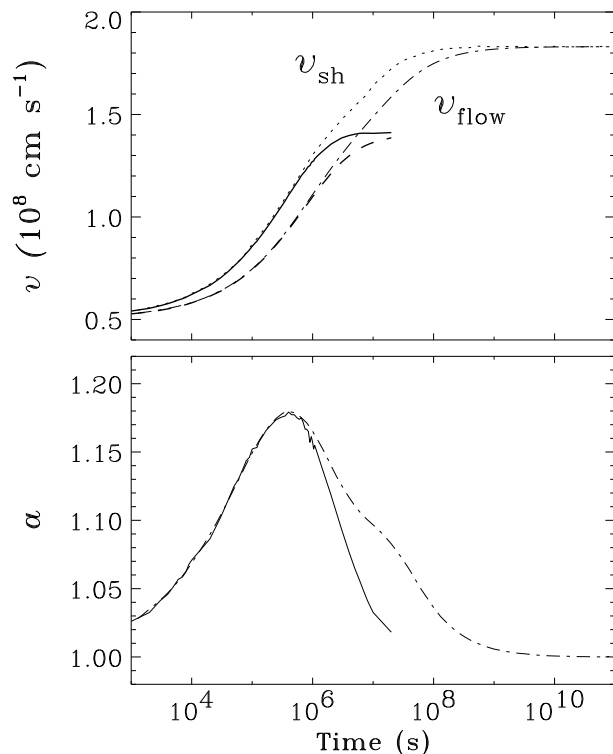


Fig. 6.— Top: Evolution of the shell velocity (left) and the flow velocity (right) at the right hand side of the contact discontinuity. Bottom: Expansion rate of the shell, $a = d\ln r/d\ln t$, equivalent to the velocity contrast between the shock and the ambient free-expanding ejecta. Solid and Dashed lines: RHD; dotted and dotted-dashed lines: HD.

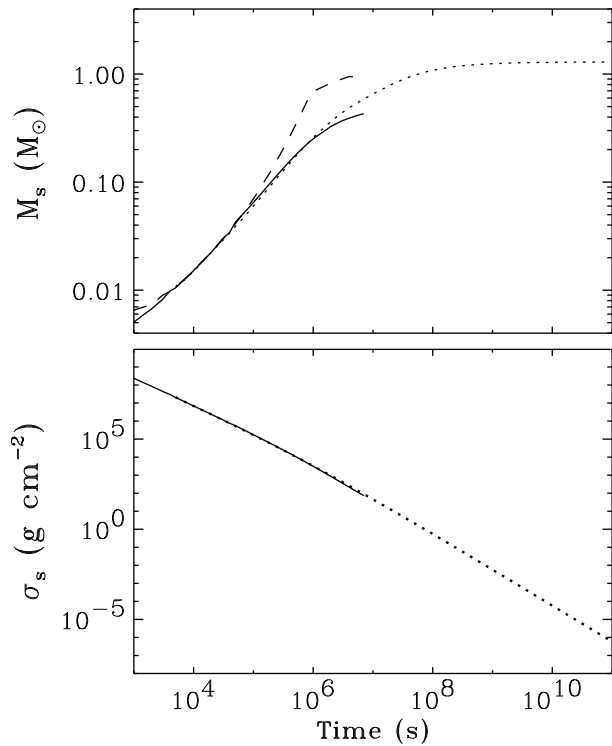


Fig. 7.— Evolution of the mass M_s and and the surface density σ_s of the shell. Solid line: RHD case, estimated within the sharp edge of the shock front; dashed line: RHD case, estimated within the radius where the shell density flattens out; dotted line: HD case.

therefore expected that the radiation relaxes before 10^8 s, given any large Ni overabundance. The shell mass is $M_s = 0.1M_\odot$ for $0.075 M_\odot$ of Ni.

The effect of radiative diffusion does not increase the density contrast of the Nickel bubble shell, as in shell formation during shock break-out in a Type II supernova where radiative energy losses by diffusion lead to a large compression that eventually limited by the gas pressure (WC01, Chevalier 1976). In the latter case, the flow behind the shock wave is being decelerated, and the immediate postshock region is being compressed. A drop in the dominant radiation pressure then is compensated by compression of the gas to the point where gas pressure becomes important, resulting in a large density enhancement. In our case, the pressure gradient has an opposite sign; the pressure decreases outward from the contact discontinuity to the shock front, and the radiative loss to the preshock gas is replenished by the energy diffusing from the bubble. The diffusion of energy ahead of the shock front leads to a weaker shock front and less compression in the shell.

3.2. Analogy to Pulsar Wind Nebulae

Chevalier (1984) has considered a constant-luminosity pulsar bubble interacting with constant density, freely-expanding supernova ejecta. We compare his self-similar solution with our hydrodynamical case, since the time evolution of the driving power is the only difference. The self-similarity exists for a power-law ejecta density $\rho \propto v^{-n}t^{-3}$ and a time-varying pulsar luminosity $L \propto t^{-l}$, when $n \lesssim 3$ and $l \lesssim 1$ (Jun 1998); the expansion law is $r \propto t^{(6-n-l)/(5-n)}$, as obtained from dimensional analysis. For a constant luminosity $l = 0$ and flat ejecta $n = 0$, $r \propto t^{1.2}$. The shock cannot be slowed down in the ejecta more than the free expansion rate, so the self-similar solutions only exist for $a \gtrsim 1$, i.e. $l \lesssim 1$.

In our solutions, the shell starts to accelerate with $a \gtrsim 1$. The evolution of the density profile can thus be compared to the self-similar solutions with varying l . In the self-similar solutions, decreasing l (i.e. increasing power input), or increasing the expansion rate, increases the shell thickness. For $l = 0$ and $a = 1.2$, we have $\beta = 0.02$. The shell thickness in our simulations shows a more complicated evolution than indicated by the measured expansion rate; the maximum expansion rate measured occurs at 6×10^5 sec, while the maximum thickness occurs at 5×10^6 sec. The first turnover in the thickness evolution seems to correlate with the change in the luminosity power index (see Fig. 8) at 5×10^6 sec; the second turnover occurs after 10^7 sec when the self-similarity breaks down because $l > 1$.

We overplot our solution at 4×10^5 sec on the self-similar solution with $l = 0.03$ in

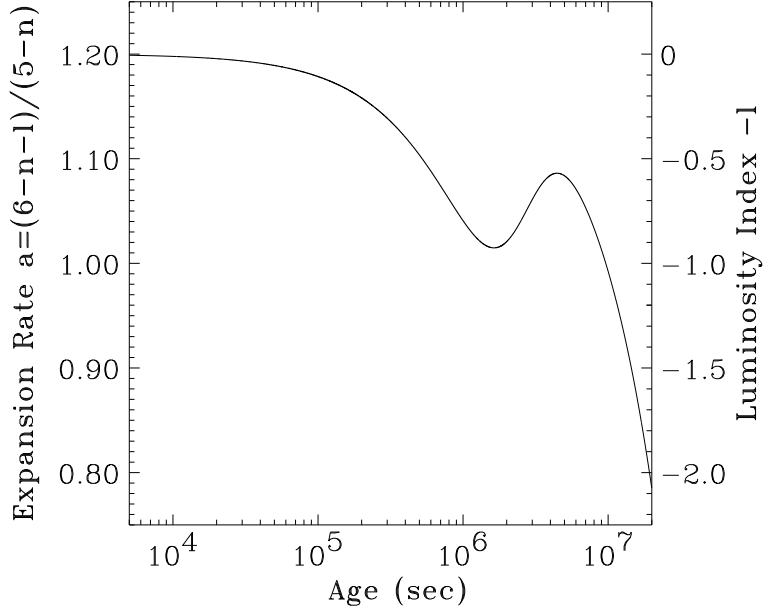


Fig. 8.— Luminosity index l of Nickel radioactivity and expansion rate a derived from the self-similar solution, $a = (6 - n - 1)/(5 - n)$.

Fig. 9. The density distribution in the shell shows a sharp inward increase towards the contact discontinuity, with over 80% of the shell mass concentrated within the inner 50% region in radius (Fig. 10). The self-similar density is infinite at the contact discontinuity. The coarseness of the grid obviously sets limits on the highest density computed in the grid domain. Our results show a higher density contrast on fixed grids, because the numerical noise is smaller than on expanding grids. The shell can be distorted by instabilities (Basko 1994; Jun 1998), but we expect the density contrast to remain comparable.

Basko's (1994, his Fig. 1) HD solutions suggest that the density contrast of the shell is only $\chi \sim 5$ at 4×10^5 sec. We reproduced his case and found that the shell broadens to $\beta > 10$ at $\sim 4 \times 10^4$ sec, the turnover is much earlier than in our results using $t_0 = 10^2$ sec. In his case, the radioactive energy accumulated to 10^4 sec was deposited all at one time, so an excessive acceleration and a large broadening were the result. Basko's Fig. 6 for the shell surface density also has the same turnover, suggesting the effect of the shell thickness.

We note that the shell characteristics such as the density contrast and the thickness ratio should only be weakly dependent on the initial Ni mass, since these properties can be approximated by the self-similar solutions.

The deformation of the bubble-shell interface due to the Rayleigh-Taylor instability is likely to have a morphology similar to that of the pulsar bubble shell studied by Jun (1998) in two-dimensional simulations. The main difference is that magnetic fields constrain the

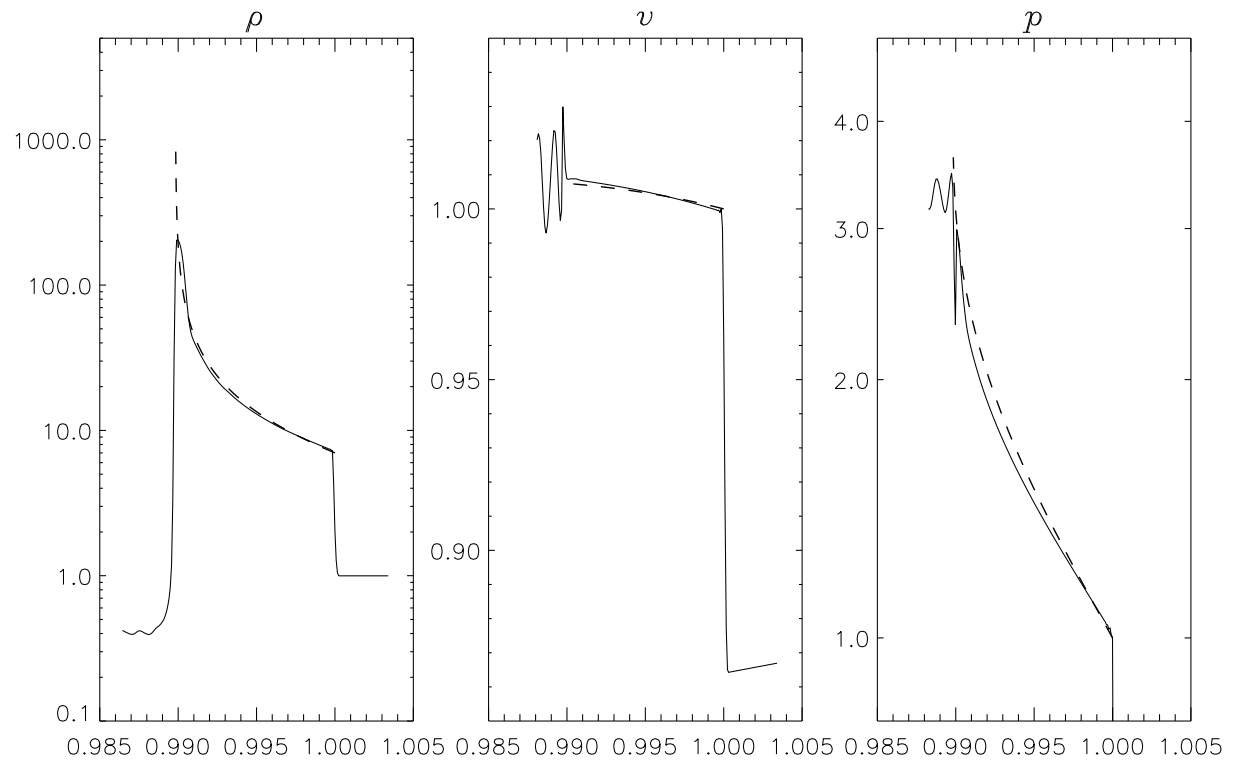


Fig. 9.— Hydrodynamical solutions of the Nickel bubble shell at 4.0×10^5 sec overplotted on the self-similar solutions of $\gamma = 4/3$, $n = 0$, $l = 0.3$, and $a = 1.14$. The velocity and pressure show large post shock oscillations behind the contact discontinuity.

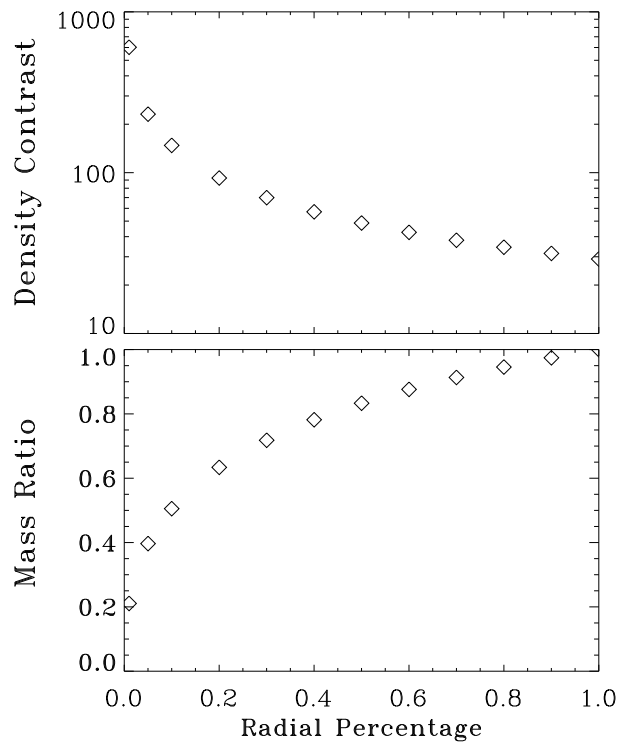


Fig. 10.— Top: Density contrast of the self-similar solution at 4×10^5 sec integrated over a radial fraction of the shell from the contact discontinuity. The innermost 1% region of the shell has an average density contrast over 600, while the total average is 20. Bottom: Integrated mass distribution.

instability in the pulsar bubble case, but are unlikely to be important for our case. The Rayleigh-Taylor spikes are directed inward, because of the shell acceleration. However, the instability should eventually end when the shell stops accelerating in the comoving stage. The effect of radiation diffusion is to smooth the pressure gradients, which ends the shell acceleration and the instability growth. The Jun (1998) simulations indicate that the instability does not cause radioactive material to have a significantly higher final velocity (see also Basko 1994).

4. NICKEL BUBBLE SHELL AS EJECTA CLUMPS

We now compare the properties of the Ni bubble shell with the initial properties of the clumps/bullets inferred from our previous clump-remnant simulations for Tycho’s remnant and the Vela supernova remnant. We consider that the ejecta clumps originate as components from the breakup of the shell. The high density contrast across the shell, $\chi \sim 100$, is compatible with that of ejecta clumps required to survive crushing in the remnant. The frozen-in velocity of the shell, $v \sim 1500 \text{ km s}^{-1}$, is also within the range $1000 \lesssim v \lesssim 3000 - 4000 \text{ km s}^{-1}$ we determined as most likely for the origin of the Vela bullets (WC02). If the shell has not been greatly disturbed, the clumps should be present in bands at the restricted velocity space; they are expected to enter the remnant’s intershock region at a normalized time $t' \sim 2.2$, or ~ 2800 yrs in our model for the Vela remnant ($M = 5 M_\odot$, and $E_{51} = 1$). The velocity-restricted nature may be revealed by the wavelike clumpy structure immediately below Tycho’s blast wave front (Reynoso et al. 1999, WC01). (see the radius and velocity plots in WC02). Comparing this set of parameters (initial density contrast, size, and ejection velocity) to that of the late clump-remnant interaction in WC02 that used a larger size $a_0 \sim 1/3$, the inferred clump strength appears insufficient to cause a protrusion on the forward shock. Nevertheless, since the computed highest density is limited by numerical resolution, a larger density contrast should be achieved in a small region. We note that for the indicated late initiation, an increase in the density contrast from 100 to 1000, compensated by a size reduction, can significantly improve the clump robustness, since the cloud crushing time scale is proportional to $t_{cc} \propto r_c^{-1/2}$ for a fixed mass (WC02, Klein et al. 1994). Such small-sized but dense clumps are very likely to form, given the steep density profile of the shell.

In our Type Ia model, the initiation of the clump-remnant interaction is expected after $t' \sim 2.0$. Still, the initiation does not give sufficient impulsion as indicated for Tycho’s knots in our previous 2-D HD simulations (WC01). The ejection occurs later than the present age of Tycho’s remnant $t' \sim 1.7$ in our model.

The swept-up mass $> 0.2M_{\odot}$ around the nickel bubble is reasonably in excess of the estimated mass $0.002 M_{\odot}$ for the Si+S clump and $0.0004 M_{\odot}$ for the Fe clump in Tycho’s remnant (Hughes 1997). For the object RX J0852 superposed the boundary of the Vela remnant, its estimated mass to account for the observed energy deposition due to clump break-out, $M \sim 0.1\beta M_{\odot}$, where $\beta < 1$, appears somewhat large compared to our standard power-law model, for which only $\gtrsim 1M_{\odot}$ can be swept into the shell. It is unclear how such a massive clump is created, if the initial Ni is not overabundant.

5. CONCLUSIONS

Our radiation hydrodynamical simulations show that the expansion of the Nickel bubble in core-collapse supernovae can sweep up a dense shell of $\gtrsim 1M_{\odot}$ shocked ambient ejecta, with the highest density in the shell over 100 times of the ambient ejecta density. The shell has an inward density increase toward the bubble-shell interface and the highest density contrast computed is limited by numerical resolution. Contrary to our expectation, radiative diffusion gives rise to a broader and less dense shell that freezes out in the ejecta around 10^7 sec. The high density contrast created can be compatible with the initial density contrast $\chi \sim 100$ of an ejecta clump required to survive the subsequent clump-remnant interaction. However, the small size $\lesssim 8\%$ in terms the intershock width, and the late ejection $v \sim 1500$ km s $^{-1}$ of the inferred clump result in a weak strength to resist crushing and further cause protrusions on the remnant outline. Multidimensional modeling that incorporates the Nickel bubble expansion with earlier instabilities would show whether such a mechanism produces the clumpy structures.

I thank T. Shigeyama for useful correspondence on Type Ia supernova ejecta. The computations were carried out on the IBM SP2 at University of Virginia. Support of this work was provided by Roger Chevalier at University of Virginia; I am grateful for his collaboration.

REFERENCES

- Aschenbach, B., Egger, R., & Trümper, J. 1995, *Nature*, 373, 587
- Basko, M. 1994, *ApJ*, 425, 264
- Chevalier, R. A. 1976, *ApJ*, 207, 872
- Chevalier, R. A. 1984, *ApJ*, 280, 797
- Chevalier, R. A., & Liang, E. P. 1989, *ApJ*, 344, 332

Dwarkadas, V., & Chevalier, R. A. 1998, *ApJ*, 497, 810

Filippenko, A. V., & Sargent, W. L. W. 1989, *ApJ*, 345, L43

Hughes, J. P. 1997, in *X-Ray Imaging and Spectroscopy of Cosmic Hot Plasmas*, ed. F. Makino and K. Mitsuda (Tokyo: Universal Academy Press), 359

Jun, B.-I. 1998, *ApJ*, 499, 282

Klein, R. I., McKee, C. F., & Colella, P. 1994, *ApJ*, 420, 213

Li, H., McCray, R., & Sunyaev, R. A. 1993, *ApJ*, 419, 824

Matheson, T., Filippenko, A. V., Ho, L. C., Barth, A. J., & Leonard, D. C. 2000, *AJ*, 120, 1499

McCray, 1993 *ApJ*, 510, 379

Reynoso, E. M., Vel'azquez, P. F., Dubner, G. M., & Goss, W. M. 1999, *AJ*, 117, 1827.

Shigeyama, T., & Nomoto, K. 1990, *ApJ*, 360, 242

Spyromilio, J. 1994, *MNRAS*, 266, L61

Stathakis, R. A., Dopita, M. A., Cannon, R. D., & Sadler, E. M. 1991, in *Supernovae*, ed. S. E. Woosley (New York: Springer) 95

Stone, J. M., Mihalas, D., & Norman, M. L. 1992, *ApJS*, 80, 819

Wang, C.-Y., & Chevalier, R. A. 2001, *ApJ*, 549, 1119 (WC01)

Wang, C.-Y., & Chevalier, R. A. 2002, *ApJ*, 574, 155 (WC02)

Winkler, P. F., Tuttle, J. H., Kirshner, R. P., & Irwin, M. J. 1988, in *Supernova Remnants and the Interstellar Medium*, ed. R. S. Roger & T. L. Landecker (Cambridge: Cambridge Univ. Press), 65

Woosley, S. E. 1998, *ApJ*, 330, 218